Deep Mantle High Viscosity and Thermochemical Structure Inferred From Mantle Flow Models Based on Seismic Tomography

Alessandro M. Forte[1] and Jerry X. Mitrovica[2]
[1] Department of Earth Sciences, University of Western Ontario
(Email: aforte@uwo.ca)
[2] Department of Physics, University of Toronto
(Email: jxm@physics.utoronto.ca)

Abstract: Surface geophysical data related to the process of thermal convection in Earth's mantle provide direct constraints on the rheological properties of the mantle. The principal convection-related data are the global-scale free-air gravity anomalies which are accurately constrained by satellite data; the observed tectonic plate motions; the dynamic topography on the core-mantle boundary (CMB), in particular the excess or dynamic ellipticity of the CMB inferred from space geodetic observations of the free-core nutation period; and the dynamic topography at the surface. Mathematical inversions of these combined data sets reveal the existence of a region of very high effective viscosity near 2000 km depth [Forte and Mitrovica, *Nature*, **410**, 1049–1056, 2001]. This inference is obtained with a viscous flow model which is based on recent high-resolution seismic models of three-dimensional structure in the mantle. The high-viscosity layer near 2000 km depth has a profound impact on the convective flow, effectively suppressing all but the longest wavelengths of flow (characterized by harmonic degrees less than about $\ell = 6$) in the deep lower mantle. As a direct consequence, the rate of flow-induced deformation in the deep mantle is strongly suppressed and hence so is the associated convective mixing. Predictions of compositional and thermal heterogeneity in this region are obtained using viscous flow calculations based on this new viscosity profile, together with independent mineral physics data. These inferences of chemical heterogeneity are in accord with the anti-correlation of anomalies in seismic shear and bulk sound velocity in the deep mantle, and they show that the mega-plumes in the lower mantle below the central Pacific and below Africa are, despite the presence of compositional heterogeneity, buoyant actively upwelling structures.

‘Acceptable’ Model of Convective Flow

Matches the convection–related data:
- global free–air gravity anomalies
- tectonic plate velocities
- core–mantle boundary topography – especially the dynamic CMB ellipticity
- dynamic surface topography

Is consistent with total mantle heat flow at surface:
- 34 TeraWatts

Is consistent with 3–D structure observed in global seismic tomographic models:
- especially the dominance of very long wavelength heterogeneity in bottom 1000 km of Earth’s lower mantle

An illustration of the dominant global scale heterogeneity in Earth’s lower mantle is provided by the following figure $\Longrightarrow$

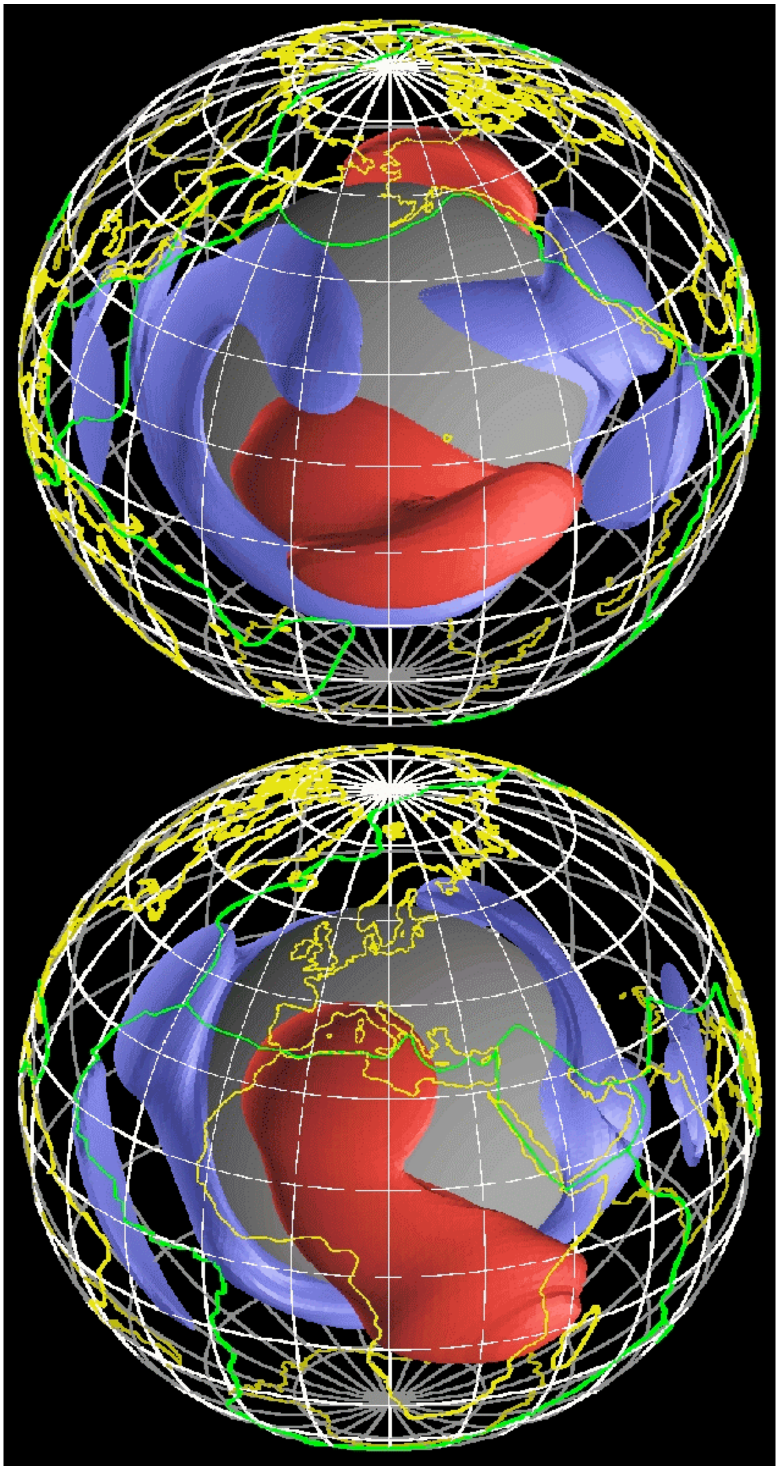

Figure 1. The three-dimensional large scale heterogeneity in Earth's lower mantle obtained by **Forte, Woodward, and Dziewonski** [model "S.F1.K/WM13", published in *J. Geophys. Res.*, **99**, 21,857–21,877, 1994]. The structure shown here was derived from a joint inversion of a large set of seismic and geodynamic data. Represented here is the shear-velocity heterogeneity synthesized from a sum of spherical harmonics truncated at degree $\ell = 4$ (the model itself contains harmonics up to degree $\ell = 8$). The red-coloured regions contain all the portions of the lower mantle in which the amplitude of NEGATIVE shear-velocity perturbations exceeds 0.7%. These regions correspond to hotter-than-average mantle. The large hot 'mega-plumes' below the central Pacific Ocean (top image) and below Africa (bottom image) are clearly visible. The blue-coloured regions contain all the portions of the lower mantle in which the amplitude of POSITIVE shear-velocity perturbations exceeds 0.4%. These regions correspond to colder-than-average mantle, and it is evident (top image) that these portions of the mantle are host to the accumulation of fossil slabs subducted along the circum-Pacific belt.

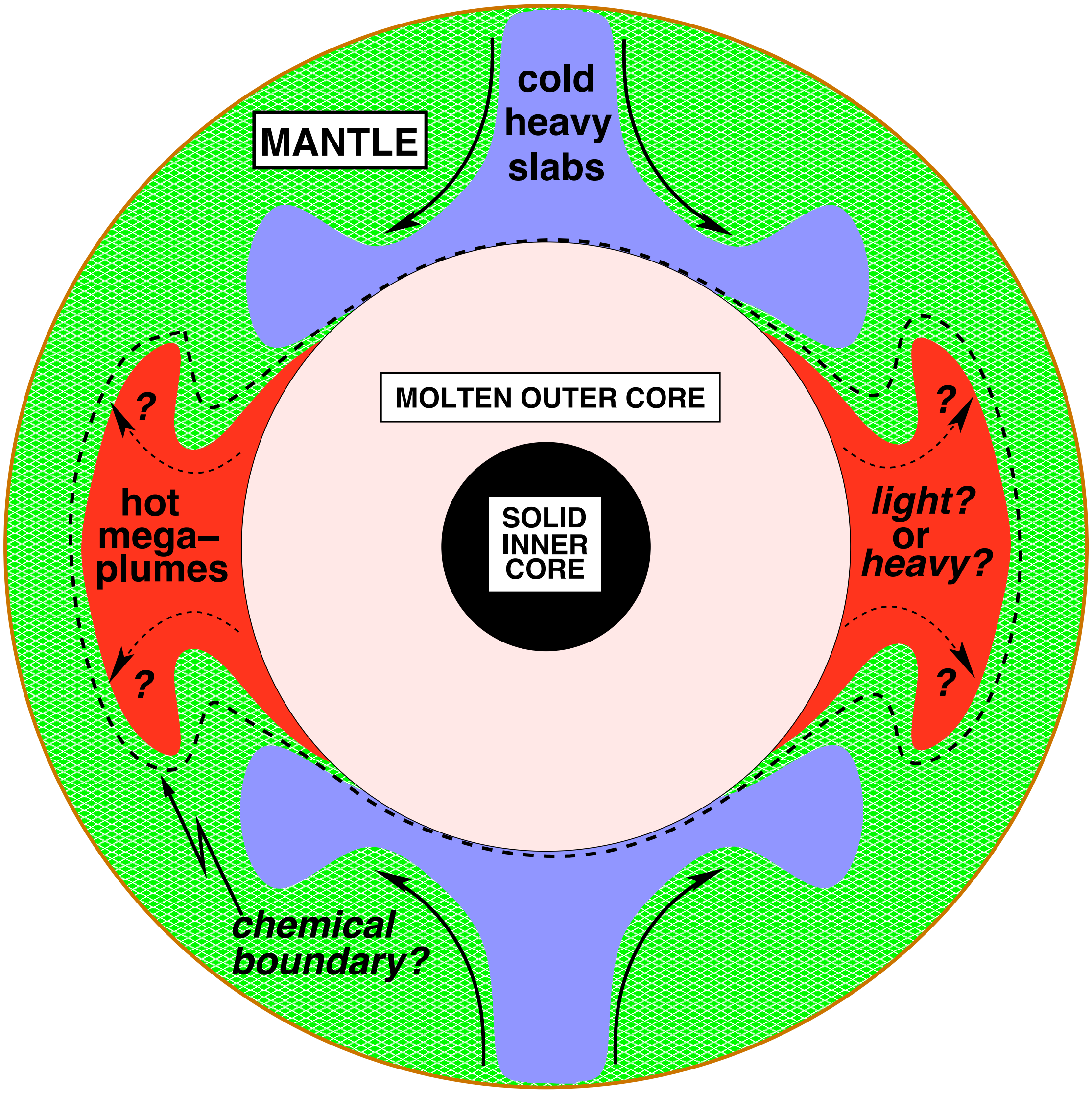

Figure 2. The large-scale lower-mantle structure in Fig. 1 may be summarized by the above schematic showing an equatorial cross-section of the mantle. While there is general agreement that slabs are cold and heavy material which descend into the lower mantle, there is no consensus regarding the dynamics of the hot 'mega-plumes'. One view is that these mega-plumes reside in primitive undepleted mantle with a major-element chemical composition which differs from the rest of the mantle. According this view, the intrinsic density due to the chemical composition of the mega-plumes cancels the thermal buoyancy due to the much hotter temperatures of these plumes [e.g., **Kellogg, Hager, and van der Hilst**, *Science*, **283**, 1881–1884, 1999]. This internal cancellation implies that the mega-plumes are stably stratified, stagnant portions of the lower mantle which do not actively contribute to mantle wide convective flow.

The difficulty presented by this scenario is that previous work on lower-mantle dynamics had shown that these mega-plumes cannot be neutrally buoyant: they must be buoyant, active upwellings in order to satisfy certain fundamental geophysical constraints, as shown in the following $\Longrightarrow$

Mantle Convection and Dynamic CMB Ellipticity

[*Forte, Mitrovica & Woodward,* Geophys. Res. Lett., **22,** 1013-1016, 1995]

Constraints on Excess Ellipticity of the Core–Mantle Boundary from Measurements of Free Core Nutation Periods

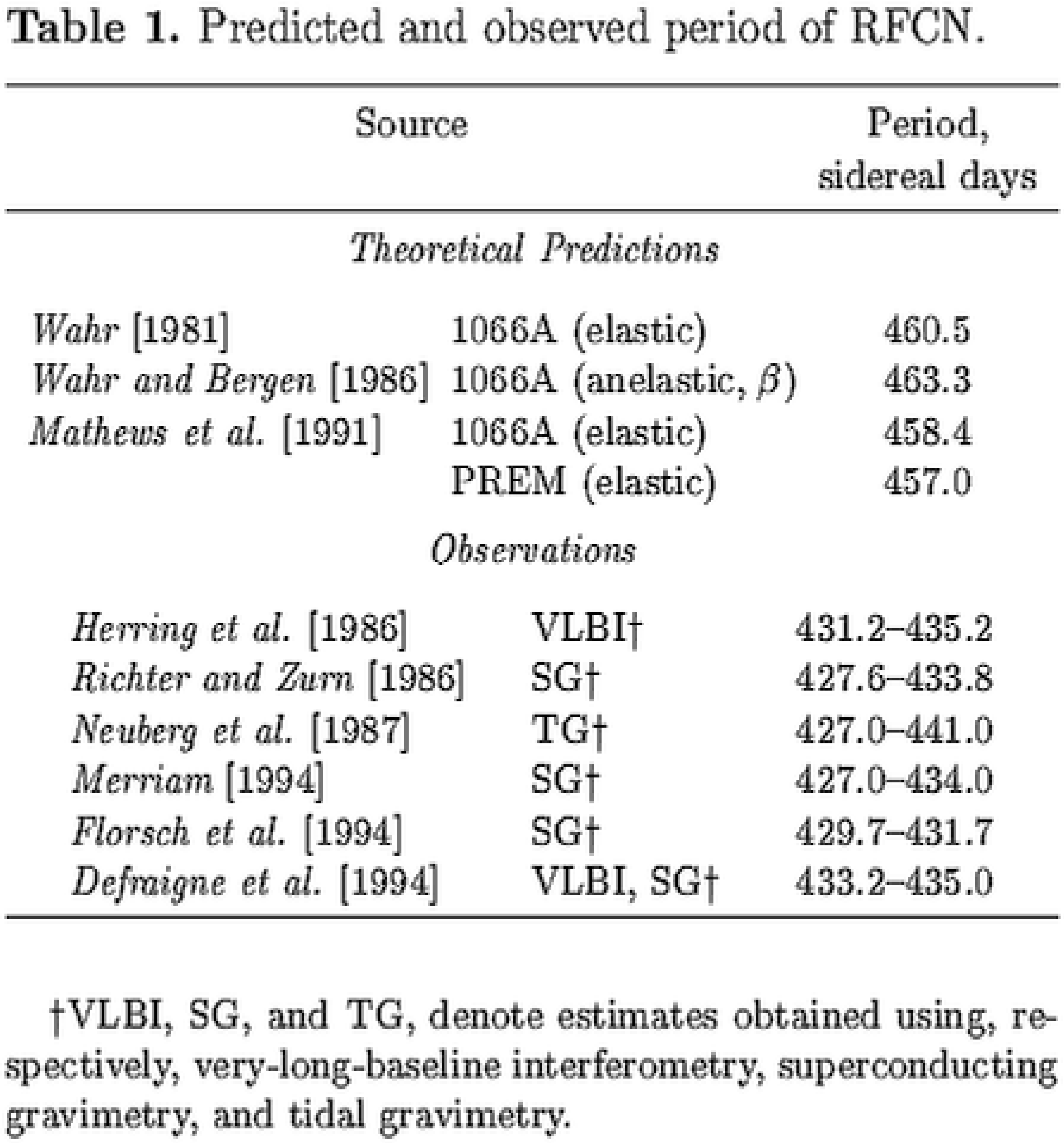

Table 1. Predicted and observed period of RFCN.

Source		Period, sidereal days
Theoretical Predictions		
Wahr [1981]	1066A (elastic)	460.5
Wahr and Bergen [1986]	1066A (anelastic, β)	463.3
Mathews et al. [1991]	1066A (elastic)	458.4
	PREM (elastic)	457.0
Observations		
Herring et al. [1986]	VLBI†	431.2–435.2
Richter and Zurn [1986]	SG†	427.6–433.8
Neuberg et al. [1987]	TG†	427.0–441.0
Merriam [1994]	SG†	427.0–434.0
Florsch et al. [1994]	SG†	429.7–431.7
Defraigne et al. [1994]	VLBI, SG†	433.2–435.0

†VLBI, SG, and TG, denote estimates obtained using, respectively, very-long-baseline interferometry, superconducting gravimetry, and tidal gravimetry.

The significant discrepancy between measured and predicted nutation periods implies an excess CMB ellipticity :

C_{20} = - 0.52 ± 0.12 km [*Gwinn et al*., 1986]

Convection induced stresses predicted using 3-D seismic models can explain this excess CMB flattening. In particular, the buoyancy forces associated with the "mega-plumes" in the bottom 1000 km of the mantle are mainly responsible for the excess CMB ellipticity.

In this study we constrain the dynamics of the lower-mantle mega-plumes by using a full suite of convection-related geophysical data, which include not only the excess CMB ellipticity but also the present-day tectonic plate velocities, perturbations in Earth's gravity field, and variations in dynamic topography at the surface. These data sets are interpreted in the context of the global scale heterogeneity in the mantle provided by two recent 'high-resolution' tomography models. Both tomography models describe the relative perturbations to seismic shear velocity, $\delta v_S / v_S$, and the first model, henceforth called model 'Grand', was derived by inverting a large number of seismic travel times [**Grand et al.**, *GSA Today*, **7**, 1–7, 1997], while the second model, henceforth called 'Ek&Dz', was derived mainly by inverting a large set of seismic waveforms [**Ekström and Dziewonski**, *Nature*, **394**, 168–172, 1998].

These two tomography models are shown in the following figure at a depth of 2740 km, corresponding to the top of the seismic D" layer $\Longrightarrow$

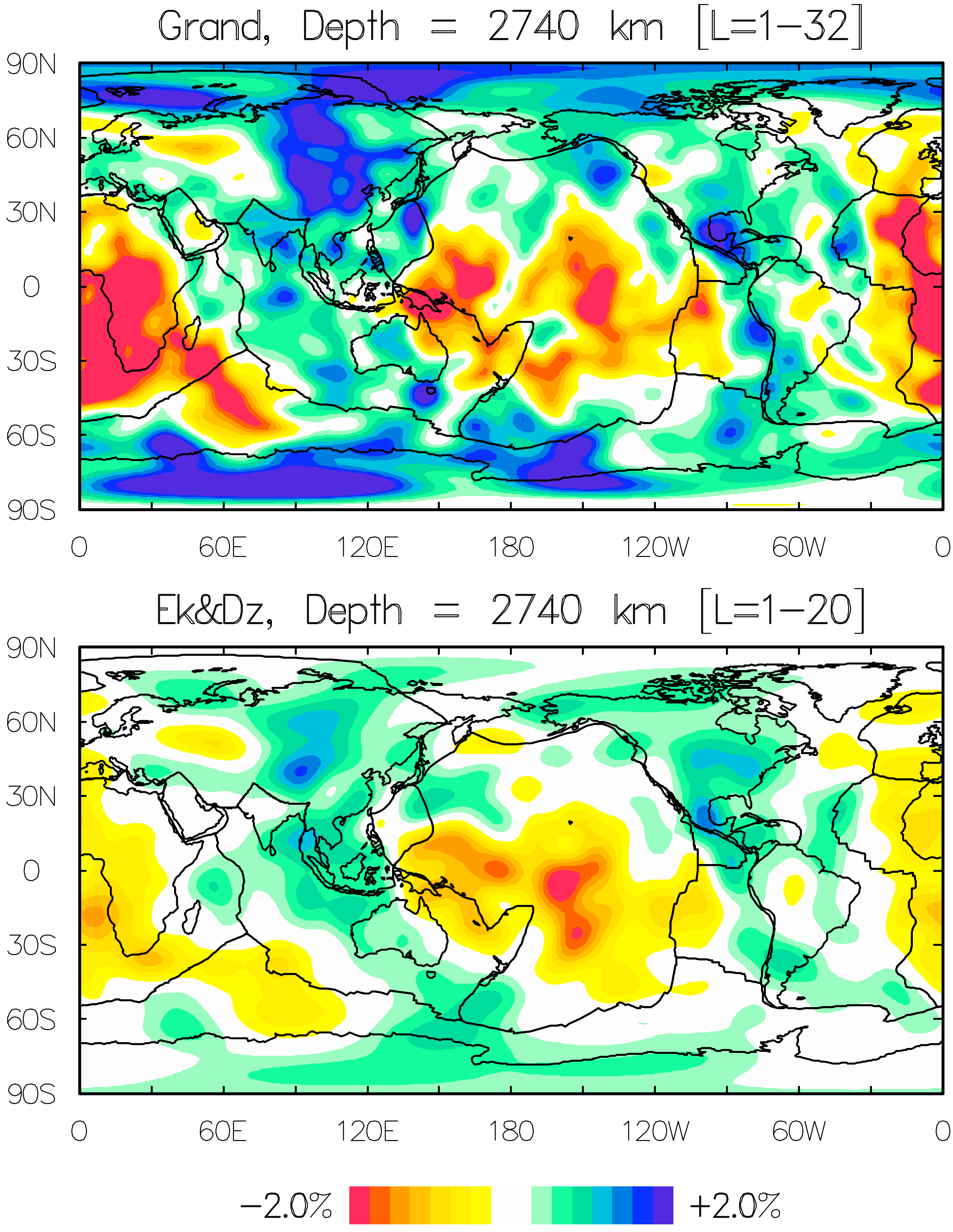

Grand, Depth = 2740 km [L=1–32]

Ek&Dz, Depth = 2740 km [L=1–20]

Figure 3.

Figure 4. We initially assumed that the shear velocity heterogeneity in these two tomography models was mainly thermal in origin. We therefore first used a velocity-to-density conversion factor $d\ln\rho/d\ln v_S$ (see black curve in figure below) based on mineral physics data [**Karato**, *Geophys. Res. Lett.*, **20**, 1623–1626, 1993] and later modified on the basis of geodynamic data [**Forte and Woodward**, *J. Geophys. Res.*, **102**, 17981–17994, 1997].

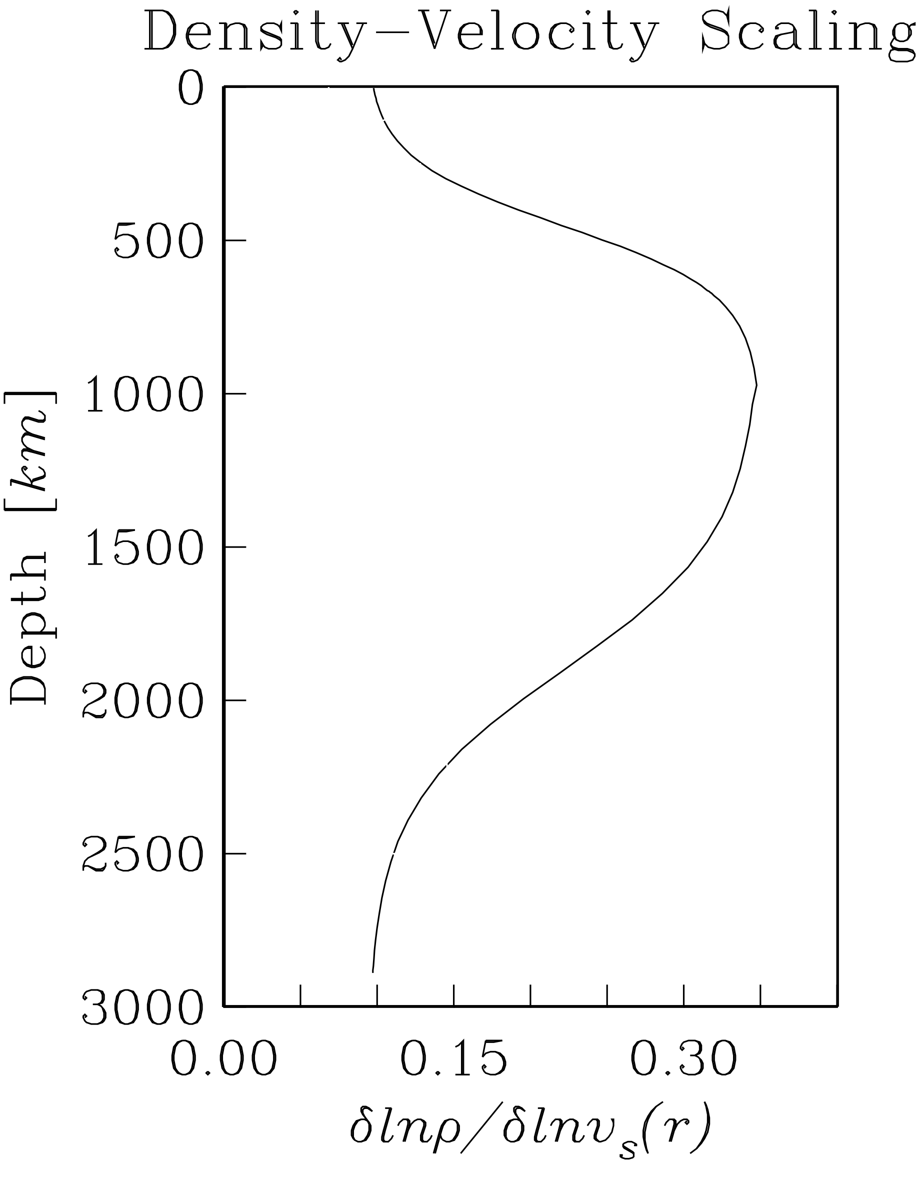

Figure 5. The mantle density heterogeneity obtained using the $d \ln \rho / d \ln v_S$ scaling (Fig. 4) is summarized by these profiles which represent the average (root-mean-square) amplitude of mantle density perturbations as a function of depth. The dashed blue curve shows the density structure derived from the Grand model and the solid black curve shows the density inferred from the Ek&Dz model. With the exception of the top 300 km, it is evident that the two models yield rather different estimates of the amplitude of density heterogeneity in the mantle. These density perturbations are of prime importance because they provide the buoyancy forces that drive the convective flow in the mantle.

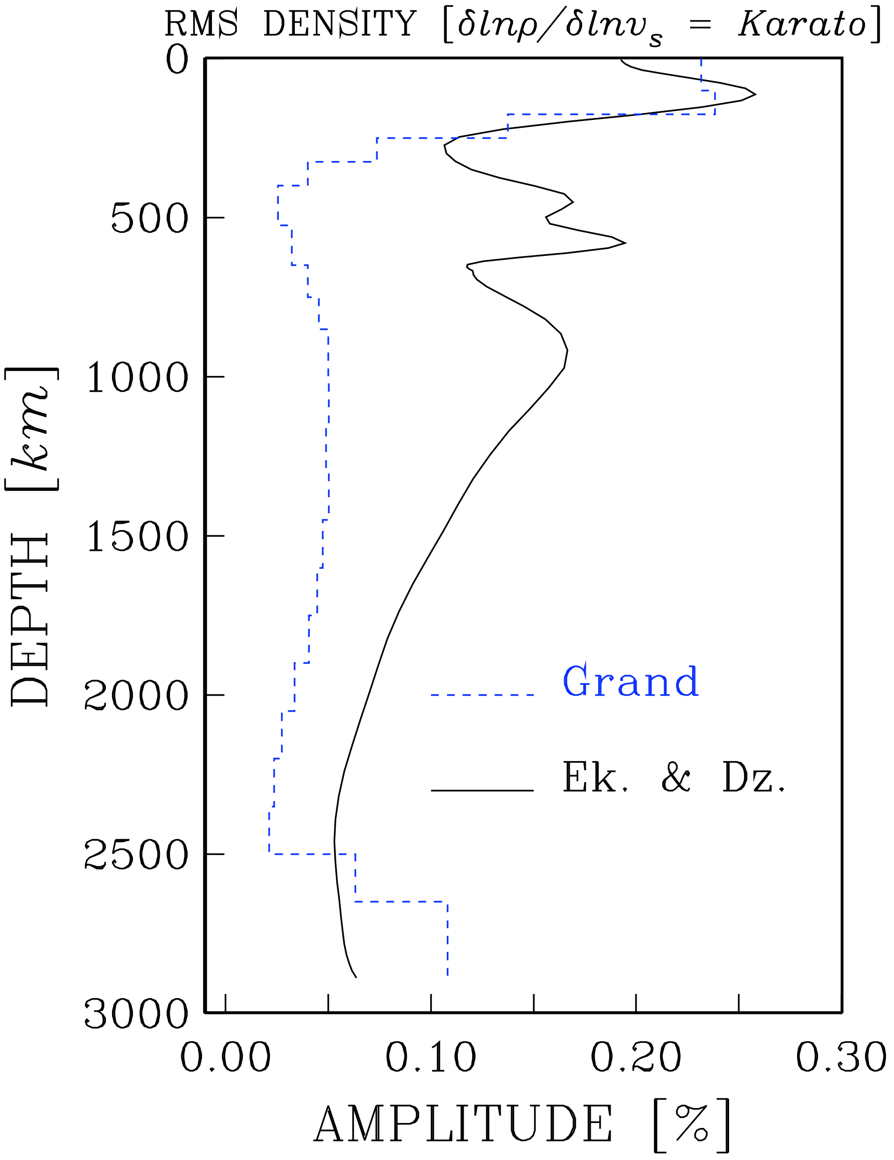

Figure 6. The second key ingredient required in the calculation of buoyancy-induced mantle flow is a model of the rheological structure of the mantle. We represent the rheology in terms of depth-dependent effective viscosity which we obtain by carrying out non-linear, iterative Occam inversions [**Constable, Parker, and Constable**, *Geophys.*, **52**, 289–300, 1987; **Forte**, in *Earth's Deep Interior, Geophys. Monogr. Ser.* **117**, S. Karato et al., Eds, AGU (Washington, DC), 3–36, 2000]. The data used are the tectonic plate velocities, the global free-air gravity anomalies, and the excess ellipticity of the CMB. The viscosity profile inferred on the basis of the density structure derived from model Grand (blue-dashed curve, Fig. 5) is represented below by the blue dashed curve while the viscosity inferred from density structure in the Ek&Dz model (black curve, Fig. 5) is represented below by the black curve. Despite the significant differences in the density structure estimated from the two tomography models, we see that the viscosity inferences are very similar.

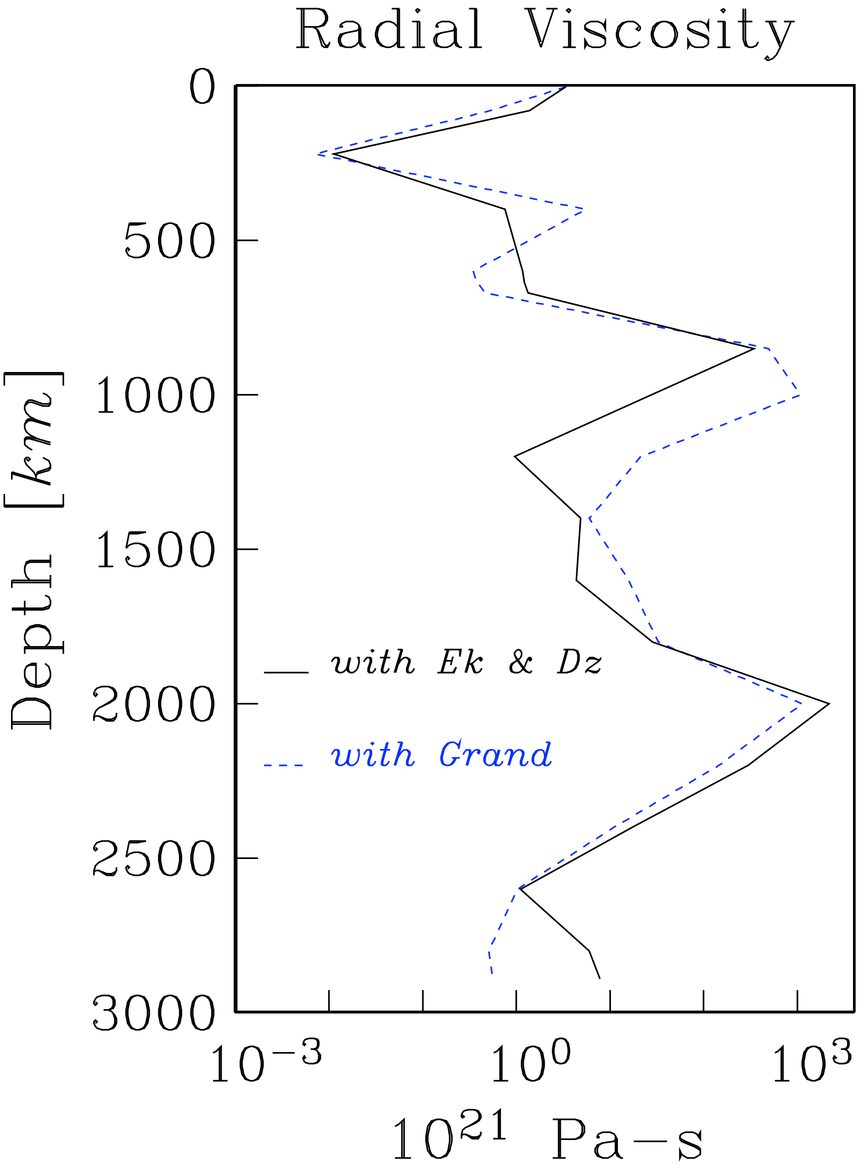

In both viscosity profiles we observe the presence of a very-low viscosity asthenospheric channel in the depth range 100–300 km, and the presence of two strong high-viscosity peaks, one near the top of the lower mantle and the other near 2000 km depth. These maxima and minima are not artifacts of the inversion since we explicitly penalize the radial roughness of the viscosity profiles. The viscosity depth dependence shown here is well constrained by the convection data.

Figure 7. We can achieve further improvements in the fit to the convection data by directly inverting for the velocity-to-density scaling coefficient rather than adopting an *a priori* scaling derived from mineral physics data. The results of an Occam inversion of the convection data for the optimal $d\ln\rho/d\ln v_S$ are shown below. The black curve again represents the modified Karato scaling (Fig. 4), while the blue and red curves show the scaling inferred on the basis of the Grand and Ek&Dz tomography models, respectively.

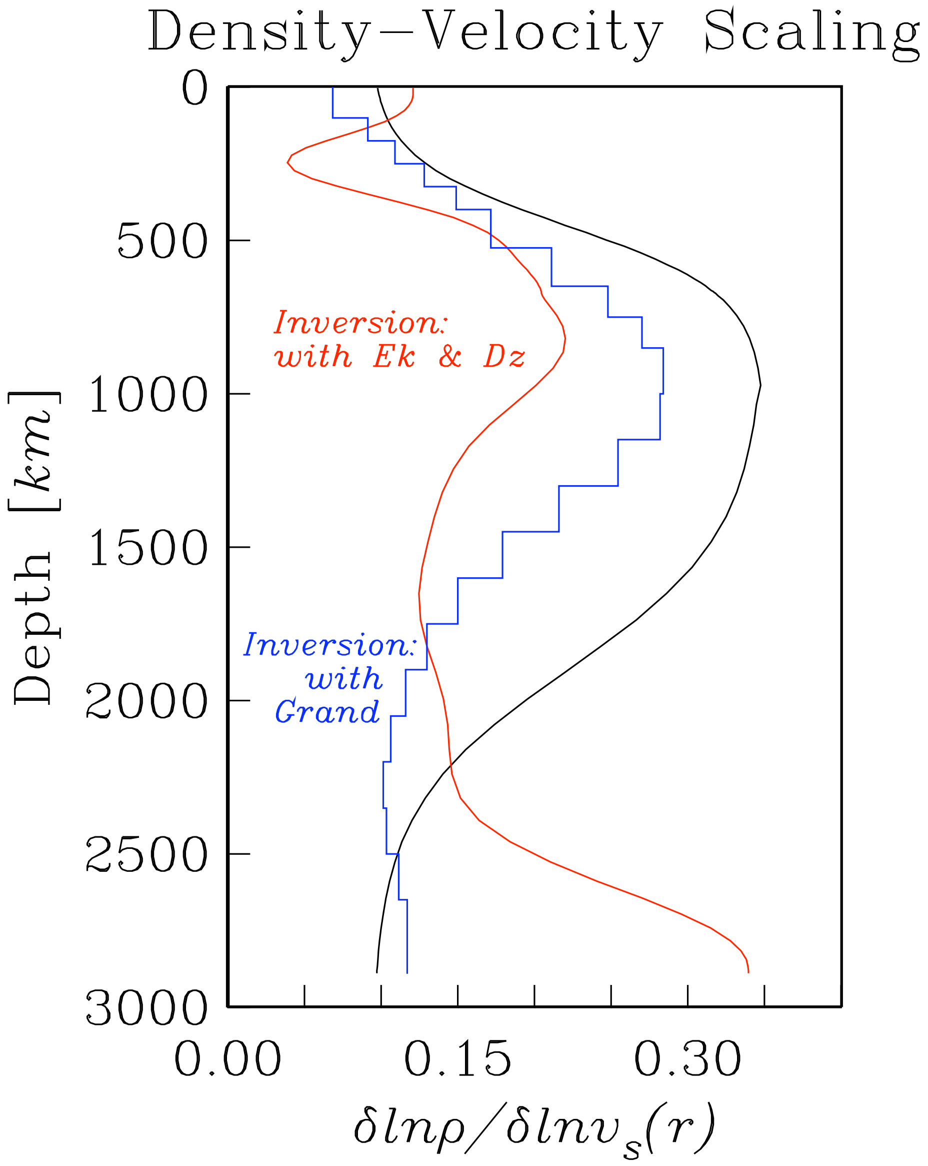

Figure 8. The average amplitude of the density perturbations derived on the basis of the newly inferred $d \ln \rho / d \ln v_S$ scalings (Fig. 7) is shown below. We note that the discrepancy (compare with Fig. 5) between the amplitude of the density anomalies derived from the Ek&Dz and Grand tomography models is significantly reduced.

This serves as an important warming: even the best mineral physics results do not allow us to properly account for the incomplete resolution of seismic heterogeneity in the tomography models. The most effective way to compensate for this difficulty, when estimating mantle density, is to directly invert the geodynamic constraints on mantle density structure.

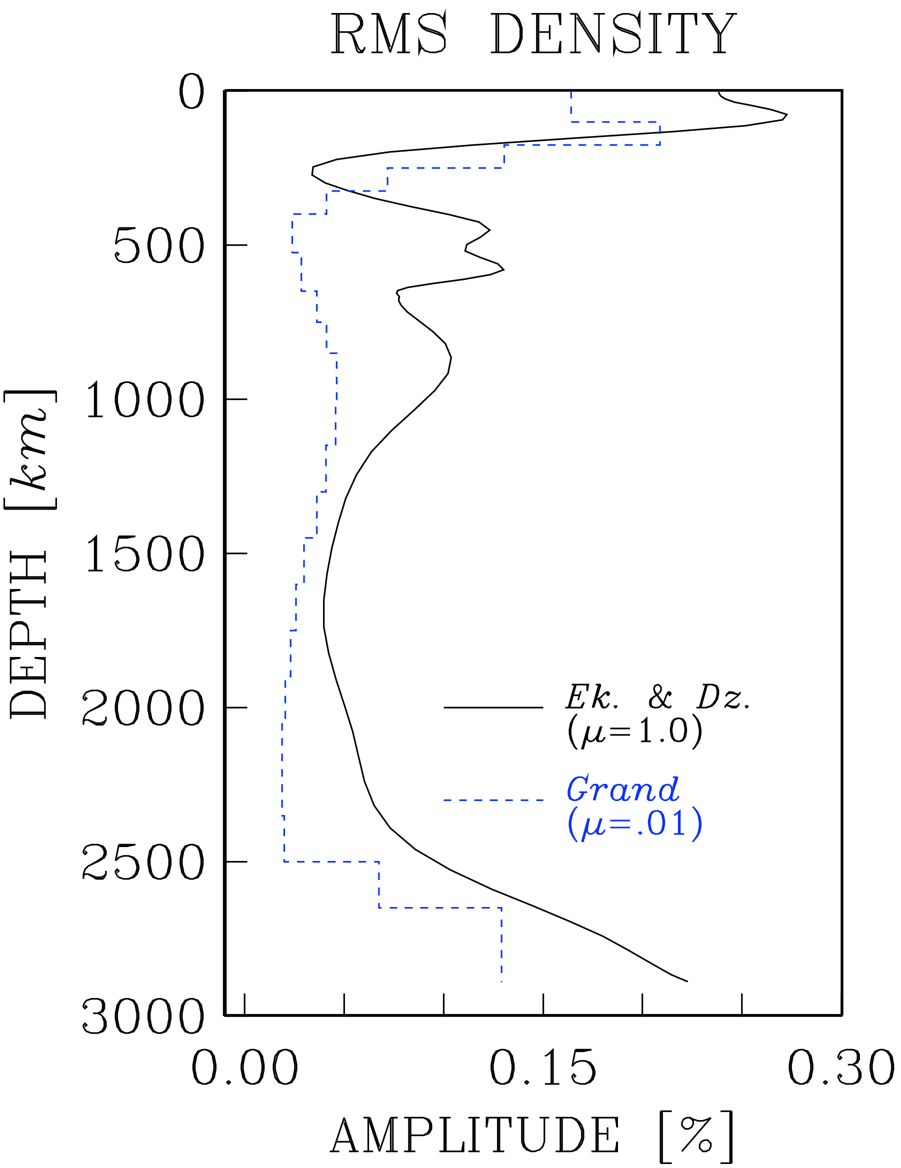

Figure 9. We now turn to a consideration of the impact of the strong increase in viscosity inferred near 2000 km depth (Fig. 6). In the figure below the black curve again represents the viscosity profile inferred on the basis of the Ek&Dz model, while the dashed blue curve is a two-layer model obtained by separately averaging the viscosity throughout the upper mantle and throughout the lower mantle.

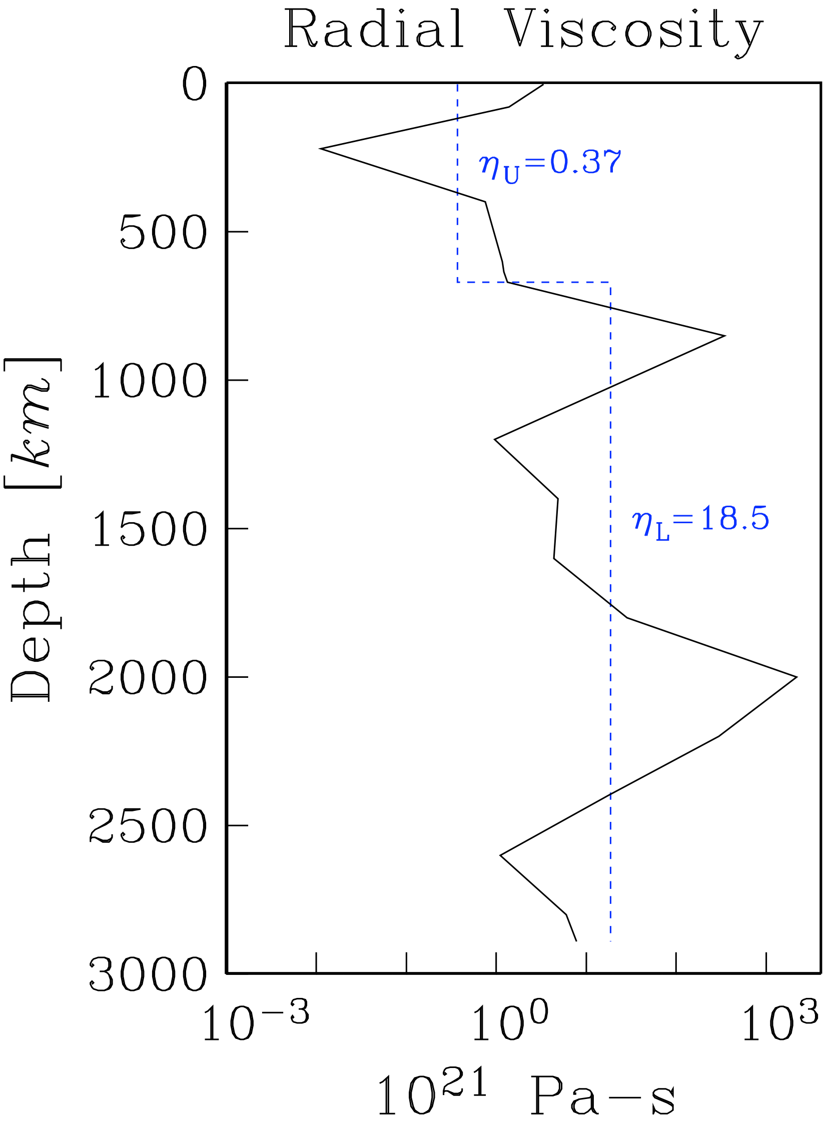

We will next compare the buoyancy-induced lower-mantle flow field predicted on the basis of these two viscosity profiles ⟹

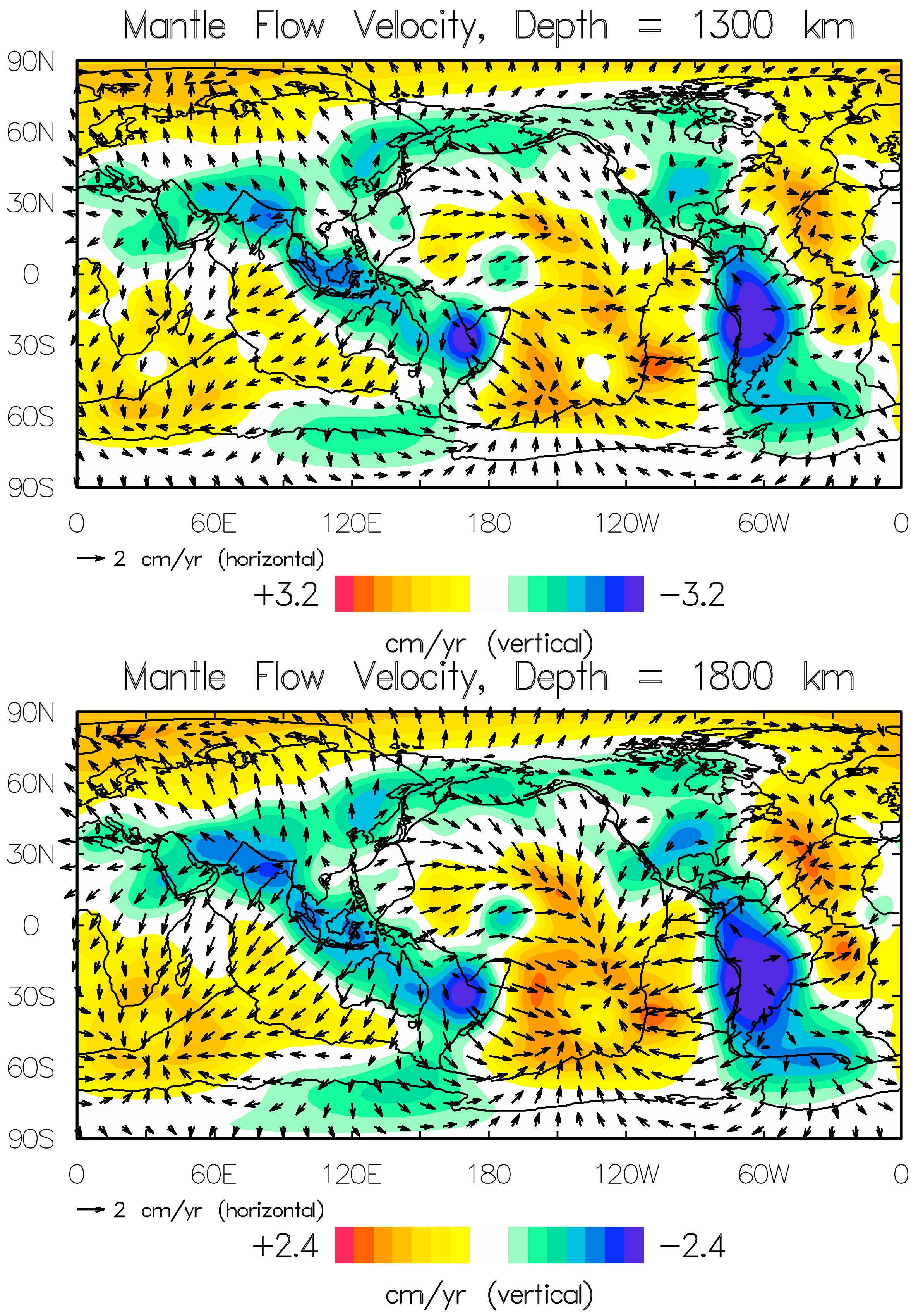

Figure 10. The mantle flow predicted on the basis of the two-layer viscosity model, using the density anomalies derived from the Ek&Dz model (black curve, Fig. 8), is shown here at two depths in the lower mantle: 1300 km and 1800 km. We immediately see that the pattern of both the vertical flow (represented by the colour contours) and the horizontal flow (represented by the black arrows) is essentially unchanged between these two depths. This is simply a consequence of the constant lower-mantle viscosity employed in this flow calculation.

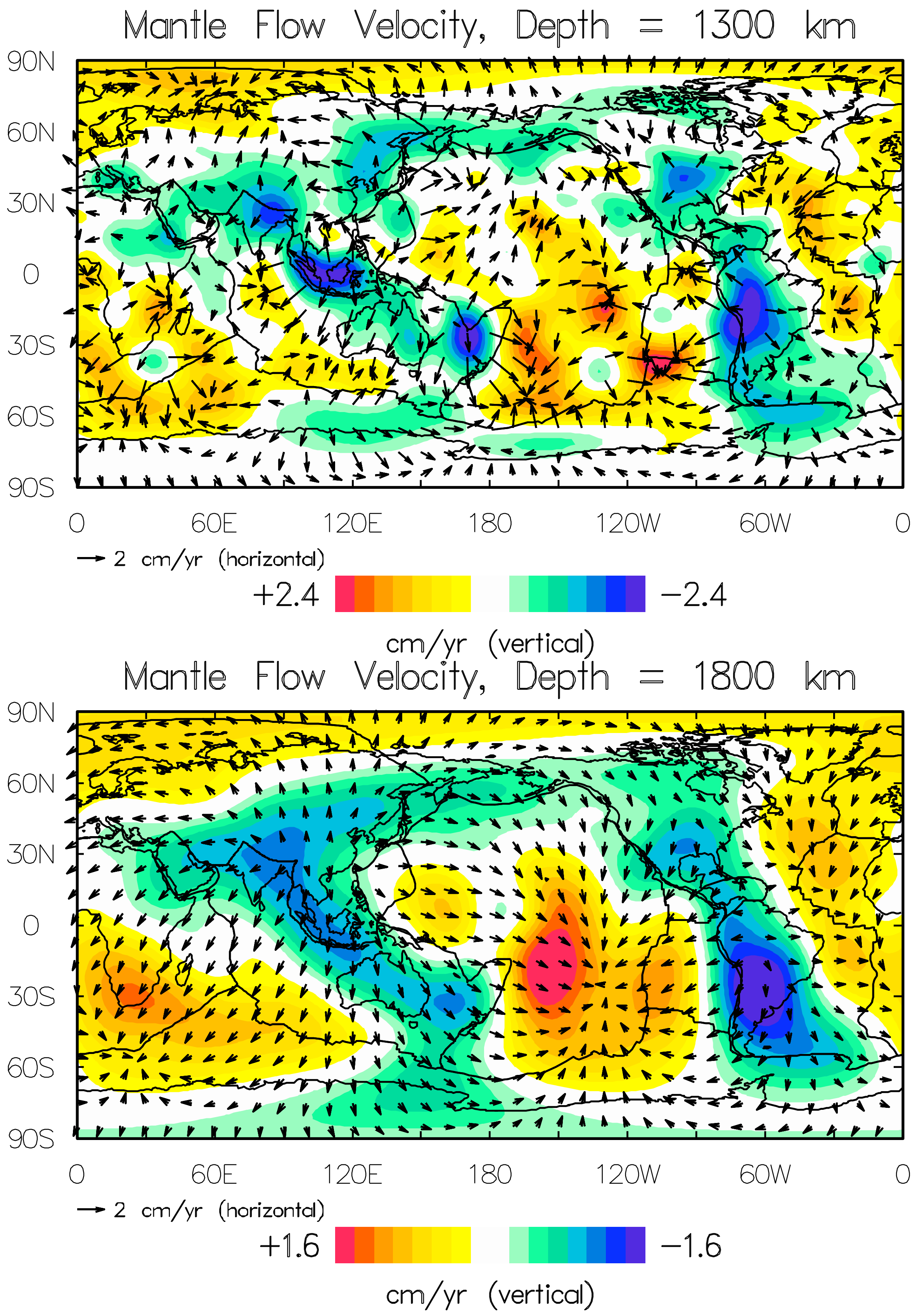

Figure 11. The mantle flow predicted on the basis of the viscosity profile (black curve, Fig. 9), derived from the inversion of the convection data, is shown here at two depths in the lower mantle: 1300 km and 1800 km. In contrast with Fig. 10, we now note a remarkable change in flow regime between these two depths. At 1300 km there is a significant amount of flow organized on shorter wavelengths. For example, we note clearly defined upwellings below Hawaii and French Polynesia. At a depth of 1800 km these individual upwellings are absent and the flow is strongly dominated by very long horizontal wavelengths.

Figure 12. The predicted mantle flow at 1800 km depth (Fig. 11) resembles the 'doming' regime, shown below, which was discovered by **Davaille** [*Nature*, **402**, 756–760, 1999] in her laboratory studies of thermochemical convection. [Figure adapted from *Nature*.]

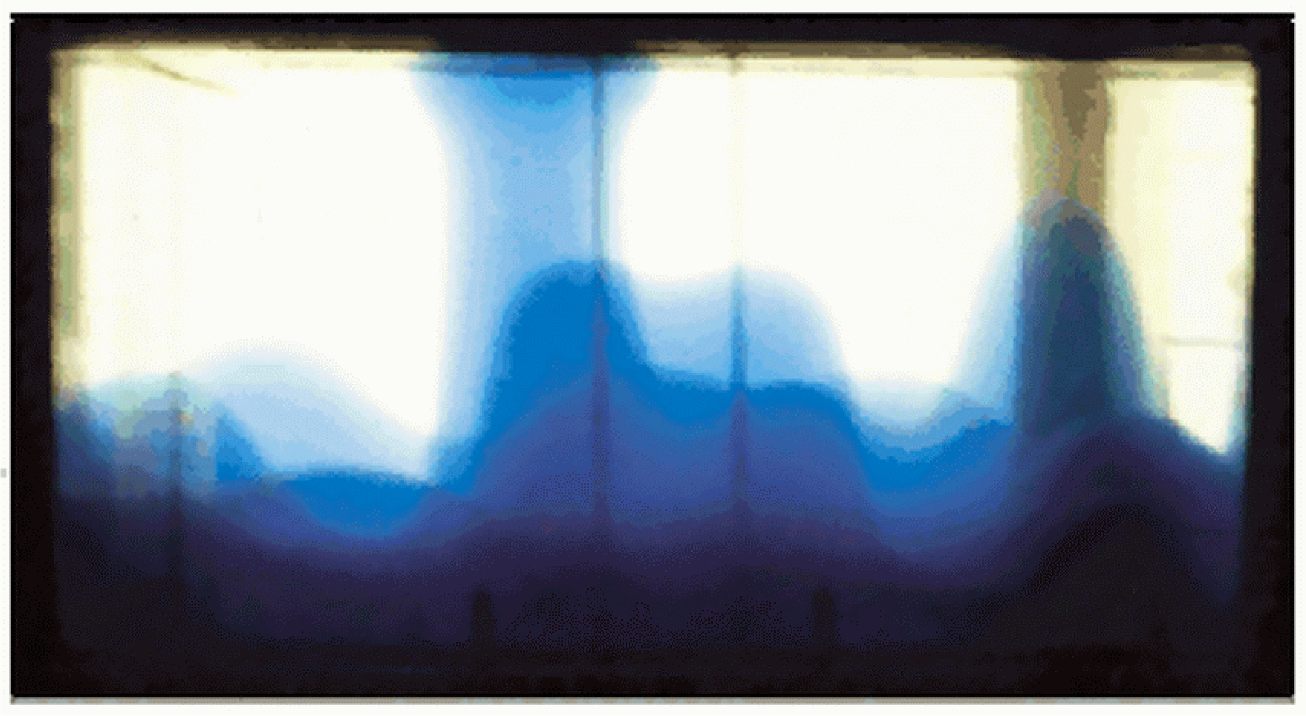

A comparison of Figs. 10 and 11, shows that the appearance of the long-wavelength 'domed' upwellings in the deep mantle are mainly a consequence of the strong increase in viscosity near 2000 km depth. Does this explanation for domed upwellings in terms of deep mantle stiffness imply that chemical heterogeneity in the lowermost mantle is unimportant? We will attempt to answer this fundamental question in the following $\Longrightarrow$

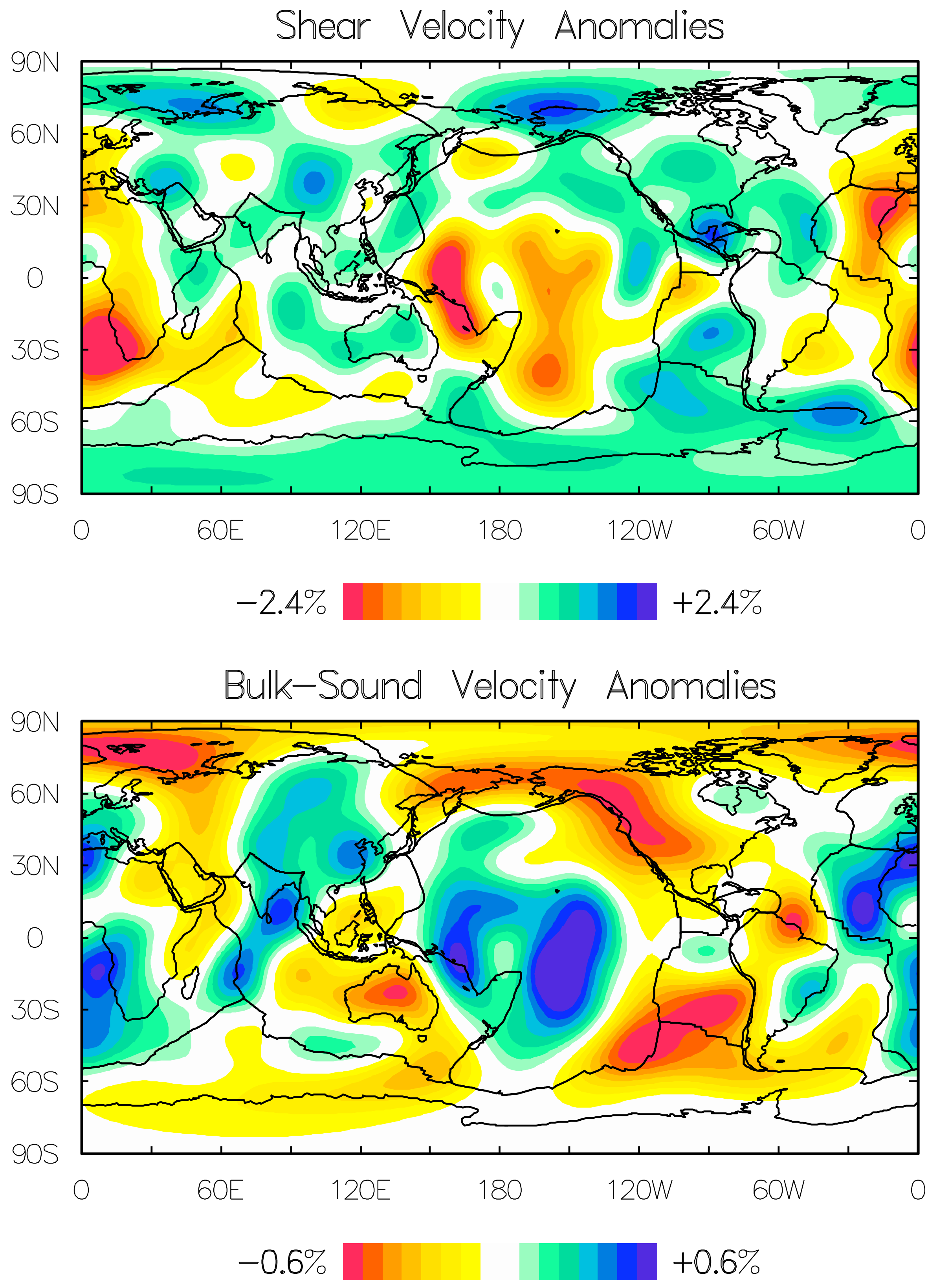

Figure 13. Over the past few years a number of seismic tomographic studies have revealed a striking anti-correlation between perturbations of seismic shear velocity, δv_S, and bulk-sound velocity, δv_ϕ. As we shall see, this anti-correlation cannot be explained by assuming that there are only lateral temperature variations in the deep mantle. In this figure we have the shear (top map) and bulk-sound (bottom map) velocity heterogeneity at the top of the seismic D'' layer (at 2740 km depth), which was obtained from the tomographic model 'MK12WM13' derived by **Su & Dziewonski** [*Phys. Earth Planet. Inter.*, **100**, 135–156, 1997].

To understand the implications of the anti-correlation between seismic shear (δv_S) and bulk-sound (δv_ϕ) velocity anomalies, we employed recent mineral physics data and theory [e.g., **Jackson**, *Geophys. J. Int.*, **134**, 291–311, 1998; **Stacey**, *Phys. Earth Planet. Inter.*, **106**, 219–236, 1998] to estimate the temperature and compositional derivatives of density ($\delta\rho$), δv_S, and δv_ϕ, at the top of the seismic D" layer (2740 km depth):

Elastic	Temperature Derivatives, $\partial/\partial T \times 10^5$ (K^{-1})	
Property	Anharmonic	Anelastic
$\ln\rho$	-1.0	—
$\ln V_s$	-4.7	-2.4
$\ln V_p$	-2.2	-0.9
$\ln V_\phi$	-0.7	0

Elastic	Compositional Derivatives	
Property	$\partial/\partial X_{Fe}$	$\partial/\partial X_{Pv}$
$\ln\rho$	+0.32	$+4.3 \times 10^{-3}$
$\ln V_s$	-0.22	+0.045
$\ln V_p$	-0.18	+0.047
$\ln V_\phi$	-0.16	+0.048

Using this Table we obtain:

$$\begin{aligned} -2.3\ \delta\ln V_s + 23.0\ \delta\ln V_\phi &= \delta X_{Pv} - 3.2\ \delta X_{Fe} \\ &\equiv \delta X_{eff} \qquad (1) \end{aligned}$$

$$\begin{aligned} (-15.5\ \delta\ln V_s + 14.5\ \delta\ln V_\phi) \times 10^3 &= \delta T + 1086\ \delta X_{Fe} \\ &\equiv \delta T_{eff} \qquad (2) \end{aligned}$$

The effective compositional heterogeneity δX_{eff} reflects lateral variations in the content of silica (via δX_{Pv}) and iron (δX_{Fe}). The effective thermal heterogeneity δT_{eff} is a combined representation of temperature perturbations and lateral variations in iron content. It turns out that:

$$\boxed{\delta T_{eff} \text{ provides an accurate approximation for } \delta T}$$

From the geodynamic inferences of $\delta\rho$ we then obtain δX_{Fe} as follows:

$$\delta X_{Fe} = 2.9\ (\delta\ln\rho + 10^{-5}\ \delta T_{eff}) - 0.013\ \delta X_{eff} \qquad (3)$$

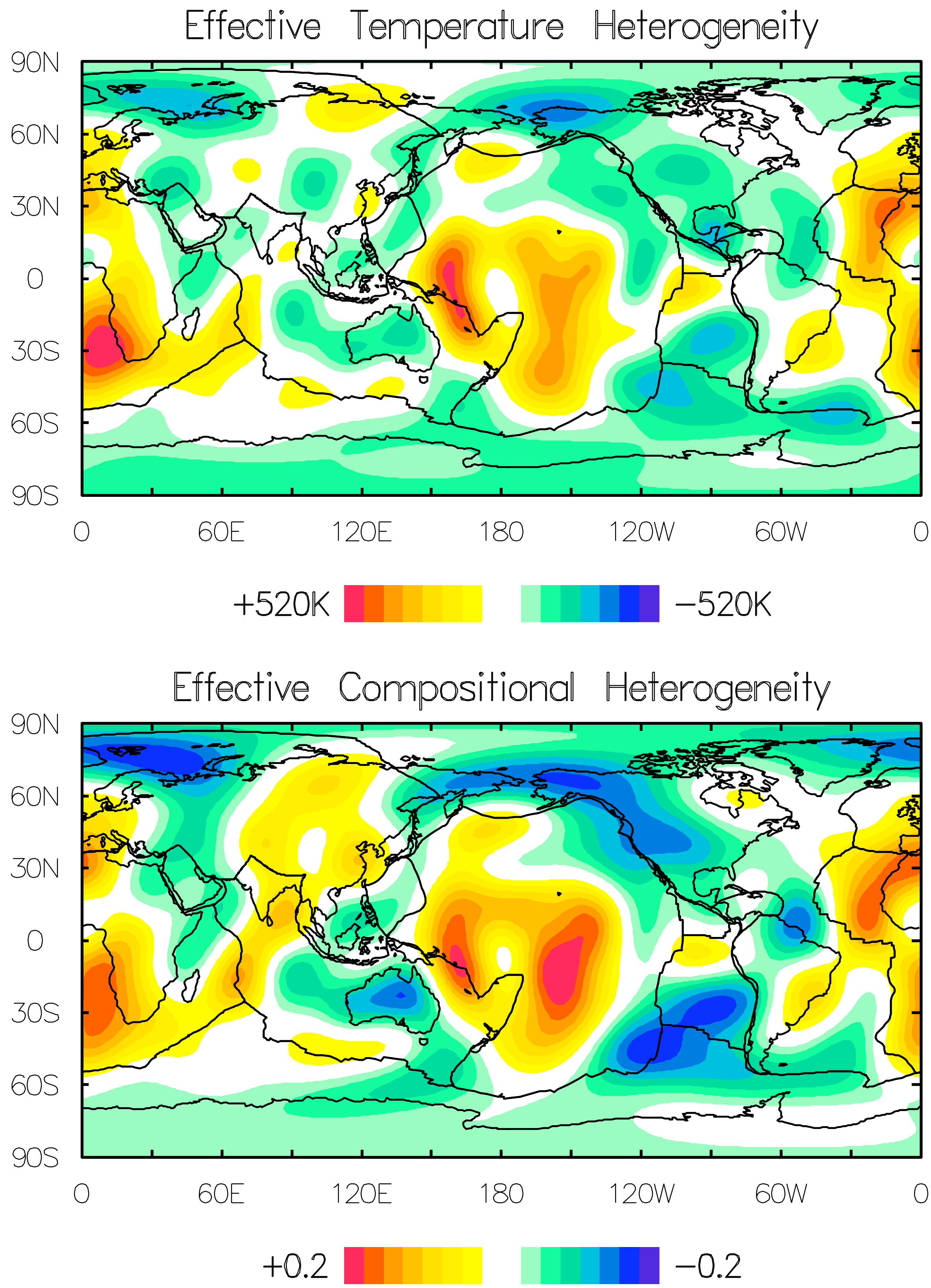

Figure 14. These maps are obtained after appling equations (1) and (2) to estimate the effective thermal and compostional heterogeneity, $\boldsymbol{\delta T_{eff}}$ and $\boldsymbol{\delta X_{eff}}$, using the velocity heterogeneity in the tomographic model MK12WM13. We note that $\boldsymbol{\delta T_{eff}}$ (top map) is strongly correlated to the shear velocity anomalies (Fig. 13, top map), while $\boldsymbol{\delta X_{eff}}$ (bottom map) is strongly correlated to bulk-sound velocity anomalies (Fig. 13, bottom map). Thus, bulk-sound velocity anomalies appear to provide an excellent proxy for compositional heterogeneity.

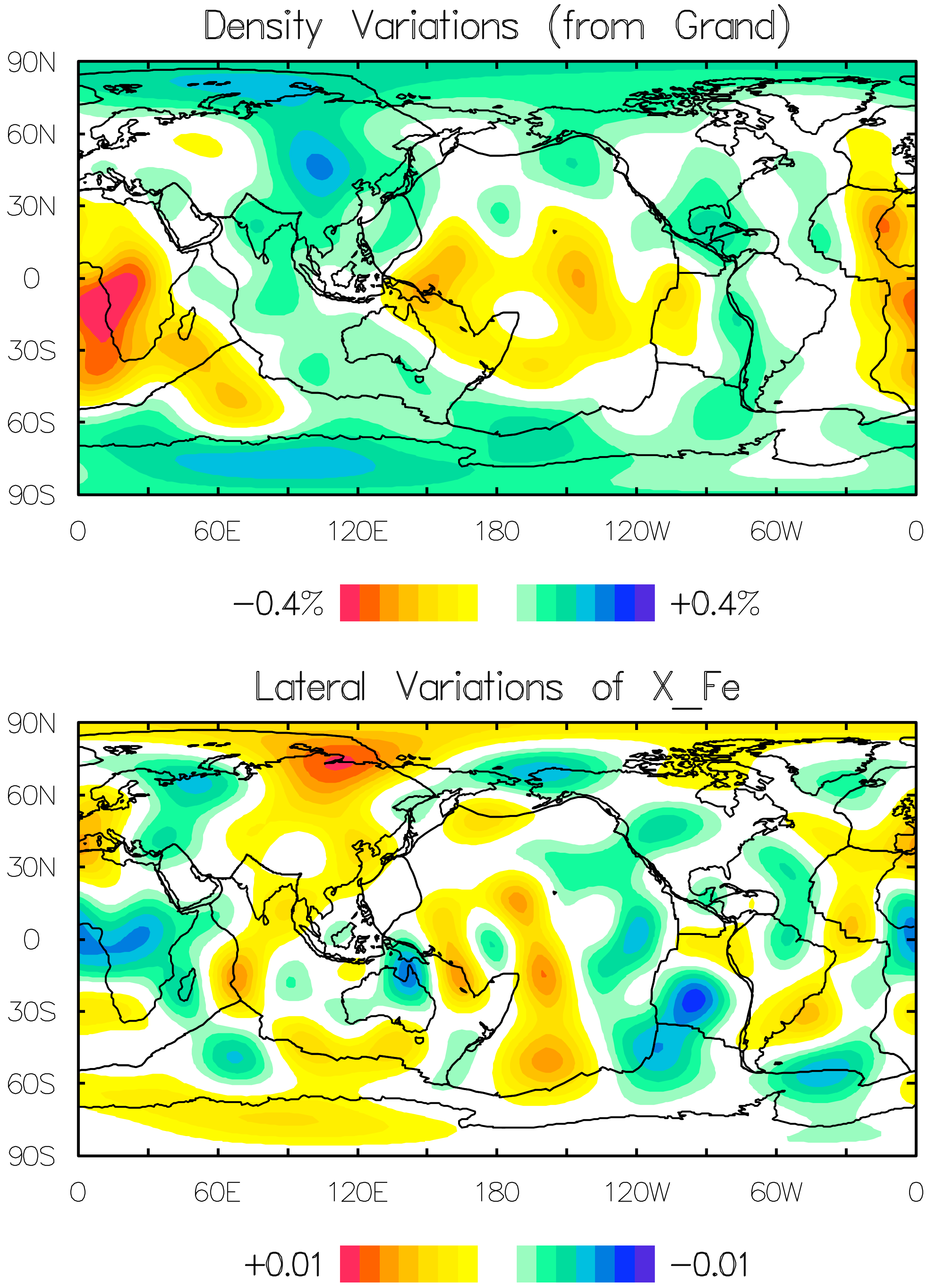

Figure 15. The top map shows the geodynamically inferred density anomalies at 2740 km depth, obtained from the Grand model (dashed blue curve, Fig. 8). The bottom map shows the corresponding lateral variation in iron content at this depth calculated on the basis of equation (3), into which we input the above density anomalies and the thermochemical heterogeneity in Fig. 14. From the amplitude of the iron heterogeneity we note that $\delta T_{eff} \approx \delta T$ is indeed a good approximation [see equation (2)].

The iron heterogeneity δX_{Fe} shown above (Fig. 15) produces associated density anomalies $(\delta \ln \rho)_{chem}$ which may cancel the pure thermal buoyancy $(\delta \ln \rho)_{th} = -\alpha\ \delta T$, where α is the thermal expansivity. The extent to which this cancellation occurs is measured in terms of a 'buoyancy ratio':

$$R_\rho = -\frac{(\delta \ln \rho)_{chem}}{(\delta \ln \rho)_{th}}$$

Employing the estimated thermal and chemical heterogeneity (Figs. 14 and 15), we calculated $(\delta \ln \rho)_{chem}$ and $(\delta \ln \rho)_{th}$ and then determined the buoyancy ratio R_ρ which provides an optimal fit between these two fields. For δX_{Fe} and δT derived on the basis of the Grand and Su & Dziewonski tomography models, we found $R_\rho \approx 0.3$. If we instead employed the density anomalies derived from the Ek&Dz model (work not shown here), we found $R_\rho \approx 0.1$. These values lie in the range of buoyancy ratios which Davaille (see Fig. 12) has associated with a distinct oscillatory doming regime for mantle convection.

Conclusions

Our analysis of the **PRESENT–DAY** dynamics of Earth´s lower has revealed that:

The radial viscosity profile inferred from global convection data possesses a low–viscosity channel in the asthenosphere (~ 200 km depth) and two high–viscosity peaks in the lower mantle near 1000 km and 2000 km depth.

The high viscosity near 2000 km depth produces a strong shift to a very long wavelength of flow at depths greater than 1600 km, with individual shorter wavelength upwelling plumes at shallower depths ***=> a red spectrum of temperature heterogeneity in bottom 1000 km of the lower mantle***

The two lower–mantle ¨mega–plumes¨ below the central Pacific Ocean and below Africa are buoyant, actively upwelling structures despite the presence of chemical heterogeneity.